

# Property Analysis of $\beta$ -Tetragonal Bismite Thin Films: Varied Concentrations and Enhanced Photocatalytic Efficiency

Hella Houda, Guettaf Temam Elhachmi, Mohammed Althamthami\*, Hachemi Ben Temam, Saâd Rahmane

\* mohammednasser132@gmail.com, mohammed.althamthami@univ-biskra.dz, mohammed.althamth1@ucalgary.ca

<sup>1</sup> Physics Laboratory of Thin Layers and Applications, Biskra University, BP 145 RP, Biskra 07000, Algeria

Received: February 2024

Revised: October 2024

Accepted: December 2024

DOI: 10.22068/ijmse.3514

**Abstract:** In this study, we thoroughly examine  $\beta$ - $\text{Bi}_2\text{O}_3$  thin films as potential photocatalysts. We produced these films using an environmentally friendly Sol Gel method that is also cost-effective. Our research focuses on how different precursor concentrations, ranging from 0.1 M to 0.4 M, affect the photocatalytic performance of these films. We conducted a comprehensive set of tests to analyze various aspects of the films, including their structure, morphology, topography, optical properties, wettability, and photocatalytic capabilities. These tests provided us with a well-rounded understanding of the films' characteristics. To assess their photocatalytic efficiency, we used Methylene Blue (MB) as a contaminant and found that the films, particularly those with a 0.1 M concentration, achieved an impressive 99.9% degradation of MB within four hours. The 0.1 M film had a crystalline size of 39.7 nm, an indirect band gap of 2.99 eV, and a contact angle of 51.37°. Our findings suggest that  $\beta$ - $\text{Bi}_2\text{O}_3$  films, especially the 0.1 M variant, have promising potential for treating effluents from complex industrial dye processes. This research marks a significant step in utilizing sustainable materials to address pollution and environmental remediation challenges.

**Keywords:** Bismuth oxide, Dip coating, Photocatalysis, Thin Films, Wettability.

## 1. INTRODUCTION

Organic dyes pose a considerable threat to environmental contamination. [1–3]. They exhibit high levels of toxicity and can be hazardous when released into the environment, posing risks to aquatic organisms, humans, plants, and animals [4]. Therefore, it is crucial to implement effective treatment of these textile effluents before their discharge into the environment [5]. Among the numerous techniques, photocatalytic technology emerges as one of the most effective methods for eliminating organic dyes. [6, 7].

In this procedure, the degradation of pollutants in water is achieved by utilizing a catalyst composed of semiconductor nanoparticles and a radiation source. Typically, ultraviolet radiation is employed, although certain studies explore the utilization of solar radiation [8], which is the reagent of choice for the process of photocatalysis due to its abundance, low cost, and environmentally friendly nature [9]. Many semiconductors such as face centered ZnO [10], CdS, MoS<sub>2</sub>, ZrO<sub>2</sub> [11], and TiO<sub>2</sub>, were used for photocatalysis [12]. Among them, Bi<sub>2</sub>O<sub>3</sub> nano-structured thin films have been proven to be valuable photo-catalyst [13]. Bismuth oxide has many advantages, including a large energy bandgap ranging from

(2 to 3.96 eV) [14], also has a high refractive index and dielectric permittivity [15]. Bi<sub>2</sub>O<sub>3</sub> generally exhibits six crystallographic phases viz  $\alpha$ -Bi<sub>2</sub>O<sub>3</sub> (monoclinic),  $\beta$ -Bi<sub>2</sub>O<sub>3</sub> (tetragonal),  $\gamma$ -Bi<sub>2</sub>O<sub>3</sub> (body-centered cubic),  $\delta$ -Bi<sub>2</sub>O<sub>3</sub> (face-centered cubic),  $\epsilon$ -Bi<sub>2</sub>O<sub>3</sub> (orthorhombic), and  $\omega$ -Bi<sub>2</sub>O<sub>3</sub> (triclinic) [16].

Moreover, heat of the stable low-temperature polymorph  $\alpha$ -Bi<sub>2</sub>O<sub>3</sub> results in the formation of the  $\delta$ -Bi<sub>2</sub>O<sub>3</sub> phase at about 730°C, which, melts at roughly 825°C. However, two transitions can occur during cooling:  $\delta$ -Bi<sub>2</sub>O<sub>3</sub> to  $\beta$ -Bi<sub>2</sub>O<sub>3</sub> at 650°C or  $\delta$ -Bi<sub>2</sub>O<sub>3</sub> to  $\gamma$ -Bi<sub>2</sub>O<sub>3</sub> at 640°C [17]. A variety of deposition methods are used to produce Bi<sub>2</sub>O<sub>3</sub> thin films, including reactive pulsed laser deposition [18], reactive pulsed laser deposition [19], dip coating [20], chemical vapor deposition [21], and hydrothermal synthesis [22]. The dip coating method is one of the low-cost and simple processing methods. It has attractive advantages including a nonhazardous and well suitable for deposition at low temperatures [20].

Methylene blue finds extensive usage in various applications, such as chemical indicators, pigments, biological staining, and more, primarily because of its affordability, solubility in water, and strong coloration [23]. This compound possesses an aromatic ring structure that is notably resistant to

natural decomposition in water samples [24]. It is crucial to emphasize that the introduction of methylene blue (MB) into the human body can lead to severe nervous system damage [25], resulting in health concerns like eye irritation, breathing difficulties, mental disorientation, vomiting, and excessive perspiration [26].

To promote the photocatalytic activity of  $\text{Bi}_2\text{O}_3$ , Wu Xiaohong et al. demonstrated that  $\text{Bi}_2\text{O}_3$  thin films obtained through a Sol-gel synthesis route and deposited via dip-coating method showed photocatalytic activity in the degradation of Rhodamine B, being this property related to the different temperatures applied during thermal treatment under UV visible irradiation [14]. H. Baqiah et al. studied the Effects of precursor concentration on the microstructural, optical, and photoelectrochemical properties of  $\text{Bi}_2\text{O}_3$  films synthesized by the sol-gel method [27]. These studies have not investigated the influence of the precursor concentration of  $\text{Bi}_2\text{O}_3$  on the photocatalytic performance of MB using the sol-gel with dip-coating method.

Within the confines of this manuscript, we have meticulously employed the Sol-gel dip-coating technique to fabricate  $\text{Bi}_2\text{O}_3$  thin films atop transparent glass substrates. The prime objective of this scholarly endeavor is to delve into the intricate interplay of precursor concentrations (0.1, 0.2, 0.3, and 0.4 M) and their consequential impact on the photonic prowess of the generated samples. This research embarks on an exploration of paramount significance: the measurement of the photocatalytic prowess of these films. Under the radiant of sunlight, their efficacy in the degradation of methylene blue is discerningly examined. To fully grasp the multifaceted

attributes of these thin films, analytical tools are meticulously orchestrated. X-ray diffraction (XRD), energy dispersive spectroscopy (EDS), scanning electron microscopy (SEM), UV-VIS spectroscopy, profilometry, and contact angle measurement collectively contribute to unraveling the nuanced characteristics of these films.

## 2. EXPERIMENTAL PROCEDURES

### 2.1. Preparation of $\text{Bi}_2\text{O}_3$ Thin Films

The following technique was used to elaborate nanostructured  $\text{Bi}_2\text{O}_3$  films:  $\text{Bi}(\text{NO}_3)_3 \cdot 5\text{H}_2\text{O}$  was dissolved in a 48.4 mL nitric acid solution (67.5% purity) with volume ratio [1:8  $\text{HNO}_3$ :  $\text{H}_2\text{O}$ ]. Then, 4 mL of polyethylene glycol ( $\text{HO}(\text{CH}_2\text{CH}_2\text{O})_{200}\text{H}$ ) was added to the solution, followed by 2 g of citric acid; the solution was stirred for 15 min before each addition, and then 0.2 mL of Triton X-100 ( $t\text{-Oct-C}_6\text{H}_4\text{-(OCH}_2\text{CH}_2)_x\text{OH}$ ,  $x=9\text{-}10$ ) as a surfactant was added drop by drop. After that, the solution was well stirred for 3h to obtain Sol solution. The sol was heated to  $60^\circ\text{C}$  for 90 min to form a gel. A schematic diagram of the sol-gel synthesis is given in Fig. 1.

The solutions have been deposited on glass substrates (MICROSCOPE SLIDES, No. 7101), with dimensions of  $(7.5 \times 2.5 \times 0.1 \text{ cm}^3)$  Glass slides were cleaned by ultrasonic cleaning in acetone ( $\text{C}_3\text{H}_6\text{O}$ ) and deionized water for 10 min each, then dried in the open air to get well-adhered and smooth films. The weight of glass substrates was measured before and after deposition solutions to measure the thickness of samples using a sensitive balance with four digits (an analytical balance).



Fig. 1. Schematic diagram of  $\text{Bi}_2\text{O}_3$  preparation by sol-gel synthesis

Following that, the glass substrates were immersed in the solution for 3 min before being withdrawn at 5 cm/min and dried at 110°C for 10 min to allow organic components to be removed. This process was repeated 10 times. The films were annealed with a heating rate of 5°C/min for 2 h at 550°C because the crystallization of bismuth oxides annealed at 550°C is better than that of bismuth oxides annealed at lower temperatures due to the crystallization of the T (tetragonal) phase of bismuth oxide [28].

## 2.2. Film Characterization

Bi<sub>2</sub>O<sub>3</sub> thin films were characterized by using different physical techniques. Bi<sub>2</sub>O<sub>3</sub> crystalline structure of the samples was characterized using grazing-incidence X-ray diffractometry (D8 Advance) using Cu K $\alpha$  irradiation of wavelength 0.15405 nm in the 2 $\theta$  range of 20–80°. The samples' crystallite size microstrain and dislocation density determined XRD from spectrum peak broadening.

The 3D surface topography and surface roughness were assessed using a Tencor P-7 mechanical profilometer, which was operated under standard environmental conditions at room temperature. This evaluation utilized the 2-bar method with a customized filter adjustment, specifically employing a Gaussian filter with a cut-off value of 0.800 m while also addressing edge effects.

The surface morphology and elemental composition were obtained by field emission scanning electron microscopy (JEOL JSM 5800) combined with energy dispersive X-ray (EDX) analysis. The surface roughness of the samples was measured by a profilometer (Tencor P-7).

Thickness measurement was carried out with the gravimetric weight difference method. The transmittance and absorbance spectra were recorded in a UV–VIS spectrophotometer (Jasco V-770) over the 300–900 nm wavelength range. Contact angle measurements are performed via the sessile drop method with IC software.

## 2.3. Contact Angle Measurement

The contact angle measurement reflects the ability of a liquid to spread over a surface by wettability. The contact angles of water drop for various bismuth thin films were measured at room temperature in an ambient atmosphere by a homemade method. A micropipette (SCILOGEX-iso 9001/13485) was used to meticulously

measure the volume of each drop (10  $\mu$ l), and the distance between the micropipette needle and the sample was fixed at 7 mm. All contact angles were averaged from five measurements with a standard deviation of approximately 5%. The average value of each drop contact angle was determined using IC software. Fig. 2 describes how the average water droplet contact angle was measured using the following equation:

$$\theta_{\text{average}} = (\theta_1 + \theta_2)/2 \quad (1)$$

Where  $\theta_{\text{average}}$  is the average angles of  $\theta_1$  and  $\theta_2$  (°),  $\theta_1$  is the angle on the left of a water drop (°),  $\theta_2$  is the angle on the right (°) [3, 29, 30].

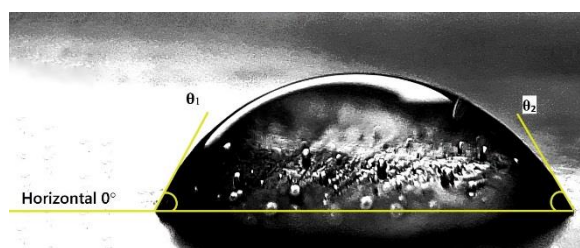


Fig. 2. The form denotes how the average value drop's contact angle was calculated

## 2.4. Preparation of the Photocatalytic Process for MB

The photocatalytic activities of Bi<sub>2</sub>O<sub>3</sub> photocatalysts were evaluated by the photodegradation of MB dye under sunlight irradiation at ~37°C. Each film with dimensions of (4.1\*2.5\*0.1 cm<sup>3</sup>) was immersed in 100 ml of MB solution (2 mg/L) for 1h in the dark to reach the adsorption-desorption equilibrium between Bi<sub>2</sub>O<sub>3</sub> particles and MB, then exposed to sunlight with stirring for 4 hours. After that, a 5 ml sample was extracted from each suspension at regular intervals (1h) using a syringe filter during the irradiation. After collecting the samples, we recorded UV-vis transmittance of the samples from 300 to 800 nm to measure the degradation of methylene blue [31].

## 3. RESULTS AND DISCUSSION

### 3.1. X-ray Diffraction

XRD technique was used to analyze the structure property of the films. The recorded XRD patterns of the deposited thin films are shown in Fig. 3(a). Moreover, XRD patterns showed that the common structure corresponds to the Tetragonal (T) phase.

**Table 1.** Data analysis summary

Crystallographic dominant Phase	Unit	Thin films with different precursor concentrations			
		0.1M	0.2M	0.3M	0.4M
		$\beta$ -Bi <sub>2</sub> O <sub>3</sub>	$\beta$ -Bi <sub>2</sub> O <sub>3</sub>	$\beta$ -Bi <sub>2</sub> O <sub>3</sub>	$\beta$ -Bi <sub>2</sub> O <sub>3</sub>
Crystal Size	nm	28.6	48.6	41.3	31.8
Surface Roughness (Rq)	nm	18.3	18.4	12.4	8.73
Film Thickness	nm	~40	~73	~83	~115
Transmission in the Visible range	%	78	68	68	63
Optical Direct Band Gap	eV	3.34	3.41	3.53	3.33
Optical Indirect Band Gap	eV	2.99	3.1	3.24	2.97
Bi Content	wt. %	18.41	22.33	23.27	31.04
O Content	wt. %	34.73	29.88	30.53	27.48
Si Content	wt. %	46.87	47.80	46.20	40.29
Average contact angle	°	51.37±2.13	45.57±2.68	67.14±3.66	61.61±3.21
MB degradation	%	~99	~96	~95	~93
Constant rate		1.00	0.81	0.76	0.71

The films (0.1, 0.2, and 0.3 M) mainly consist of monoclinic and tetragonal phases, which are labeled M and T, respectively. At 0.4 M film, a new peak appeared corresponding to the cubic phase, which has been reported by Wu Xiaohong et al. [14]. The average crystallite size of the Bi<sub>2</sub>O<sub>3</sub> thin films was estimated using the full width at half maximum (FWHM) from the line broadening of the tetragonal orientation. The average crystallite sizes were calculated using the Scherrer formula:

$$D = k \lambda / \beta \cos \theta \quad (2)$$

where D is the crystal diameter, k is the Scherrer constant and is taken equal to 1,  $\lambda$  is the wavelength of the X-rays, and  $\beta$  is the full width at half maximum (FWHM) of X-ray diffraction peaks in radians [32]. The average crystallite size of the Bi<sub>2</sub>O<sub>3</sub> films prepared by molar precursors of 0.1, 0.2, 0.3, and 0.4 M was found to be 506, 480, 407, and 360 nm, respectively.

$$(\varepsilon) = \beta \cos \theta / 4. \pi \quad (3)$$



**Fig. 3.** a) XRD spectra of bismuth oxide films prepared by different precursor concentrations. b) The variation of crystallite size, lattice strain, and dislocation density as a function of the molar concentration of precursor



The dislocation density ( $\delta$ ), which represents the amount of the defect in the sample, is defined as the length of dislocation lines per unit volume of the crystal [33], and is calculated using the following relation [34]:

$$(\delta) = 1/D^2 \quad (4)$$

The structural parameters such as crystallite size, strain ( $\epsilon_{\text{average}}$ ), and dislocation density ( $\delta_{\text{average}}$ ) are listed in Table 2. The variation of these parameters was a function of the molar precursor, as shown in Fig. 3(b).

It was noticed that the crystallite size varies (from 286 to 486 nm) and has an inverse relation with the full width at half maximum FWHM. The small value of ( $\delta$ ) obtained in the present study confirmed the good crystallinity of the  $\text{Bi}_2\text{O}_3$  thin films [35]. A direct correlation exists between dislocation density (from  $9.88.10^{-6}$  to  $1.22.10^{-5}$ ) FWHM and strain since more strain creates more dislocations in the crystal structure. This result is in agreement with the previously reported [36].

### 3.2. $\text{Bi}_2\text{O}_3$ Thin Films Morphological and 3D Surface Topography

The surface morphology of  $\text{Bi}_2\text{O}_3$  films (from 0.1 to 0.4 M) was carried out using a Scanning Electron Microscope (SEM), as shown in Fig. 4(a-d), respectively. All the films have irregular island morphology with good overall coverage. Fig. 4a shows isolated islands that are not clustered with each other. When the precursor concentration is increased, the island grains' size increases; this is due to accumulation in thicker film, resulting in grain growth as shown in Fig. 4(b) and slightly decreases until the film surface appears as big grains that

are more compact and denser, as shown in Fig. 4(d).

The result of cross-sectional SEM images supports the XRD patterns that increase the intensity of all diffraction peaks, which is influenced by the thickness of the film. Which is in good agreement with the reported [37]. A quantitative surface topography analysis was performed using stylus profilometry data. The investigated parameters include the average roughness, Ra, which is the arithmetic average height from a mean line over some evaluation length L; the second parameter is the root-mean-square roughness, Rq, indicating the geometric average height measured from a mean line within the sampling length L; Rt denotes the third parameter and corresponds to the distance between the highest peak and deepest valley of the profile within the evaluation length L) [38]. The roughness parameters Ra, Rq, and Rt of different precursor concentrations are shown in Table 3. Figs. 4 and 5 indicate that Rq values ranged from 8.73 to 18.3 nm, which are slightly higher than Ra (6.66 to 14.2 nm) values, indicating that the average amplitude from the mean line is higher than the average of peaks and valleys in the height direction.

The highest roughness values (18.4 and 18.3 nm) correspond to the compounds deposited with 0.2 and 0.1 M films, which increase the photocatalytic efficiency. The lower roughness values were 9.44 nm and 6.66 nm, corresponding to 0.3 and 0.4 M films. Larger surface grains of prepared films engendered a rougher surface feature-similarly, a substantially increased surface grain size, as reported in the ZnO film [39].

**Table 2.** The structural parameters of various concentration precursor  $\text{Bi}_2\text{O}_3$  thin films

Precursor concentration	Position $2\theta(\text{deg})$	d spacing	FWHM $B_T(\text{deg})$	D(nm)	$\delta$ dislocation density ( $\text{nm}^{-2}$ )	$\epsilon$ lattice strain
0.1M	29.28	3.05	0.29	286	$1.22.10^{-5}$	0,49
0.2M	29.51	3.06	0.17	486	$4.23.10^{-6}$	0,29
0.3M	29.27	3.05	0.20	413	$5.86.10^{-6}$	0,34
0.4M	29.43	3.03	0.26	318	$9.88.10^{-6}$	0,44

**Table 3.** 3D surface topography roughness analysis and shape parameters for  $\text{Bi}_2\text{O}_3$  thin films

Roughness profile (nm)	Precursor concentration (M)			
Parameters	0.1	0.2	0.3	0.4
Rt (nm)	116	130	97.3	63.4
Rq (nm)	18.3	18.4	12.4	8.73
Ra (nm)	14.2	13.6	9.44	6.66



**Fig. 4.** SEM images and EDS spectrums of  $\text{Bi}_2\text{O}_3$  films synthesized by the different precursor concentrations: (a2) 0.1, (b2) 0.2, (c2) 0.3, and (d2) 0.4 M

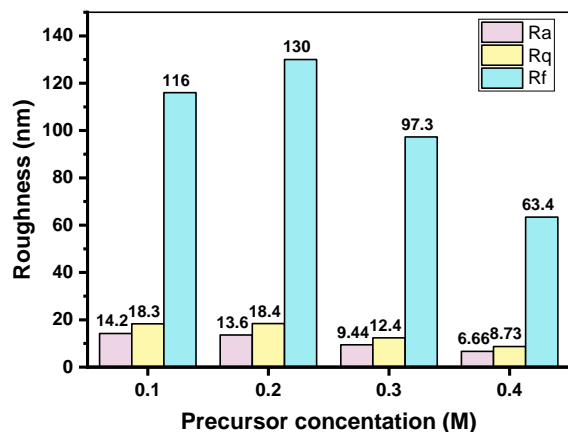


**Fig. 5.** The roughness parameters Ra, Rq, and Rt of  $\text{Bi}_2\text{O}_3$  films prepared at various molar concentrations

### 3.3. $\text{Bi}_2\text{O}_3$ Thin Films EDS Analysis Patterns

The EDS compositional analysis of bismuth thin films at different precursor concentrations is shown in Fig. 4(a–d), respectively. This spectrum confirms the presence of Bi and O elements in the films. The results also indicate the presence of Si, which is attributed to the substrate glass used [40]. The Bi content increases (from 18.48 to 27.48 wt.%) as the molar concentration increases from 0.1 to 0.4 M, attributed to a rise in its atomic percentage. Whereas the decrease in oxygen content (from 34.73 to 27.48 wt.%) could be due to the chemisorbed oxygen from the atmospheric air [41].

### 3.4. Spectral Analysis UV-Visible

The optical properties of  $\text{Bi}_2\text{O}_3$  thin films

prepared using various precursor concentrations were studied by UV–visible spectrophotometer in the 300–900 nm range at room temperature, as depicted in Fig. 6(a). As noticed, the transmittance increases with increasing wavelength, and its average value in the visible region of the spectrum is (78, 67.66%, 67.68%, and 63%); in the ultraviolet region, it is (51, 32, 34%, and 18%), with rising precursor concentrations (from 0.1 to 0.4 M), respectively. The transmittance can be associated with the grain size, RMS, porosity, and thickness of the films. It is generally expected that increased thickness and surface roughness lead to reduced transmittance while decreasing porosity and grain size decrease transmittance [42]. The gravimetric weight differential (weight increase method) was used to determine the thickness of the  $\text{Bi}_2\text{O}_3$  films.

$$D = \Delta m / A \cdot \rho \quad (4)$$

Where  $\Delta m$  is the mass difference in grams,  $A$  is the area of deposited films in  $\text{cm}^2$ , and  $\rho$  is the density of the deposited material ( $\text{Bi}_2\text{O}_3 = 9.17 \text{ g/cm}^3$ ) [43]. Fig. 6(d) shows the average thickness variation as a function of concentration precursor values. The film thickness increased (from 40 to 115 nm) as the precursor concentration increased (from 0.1 to 0.4 M) due to the high viscosity of the solution. The absorption coefficient  $\alpha$  of the mentioned films was obtained via the following equation:

$$\alpha = \ln I_0 / I \cdot 1/d \quad (5)$$

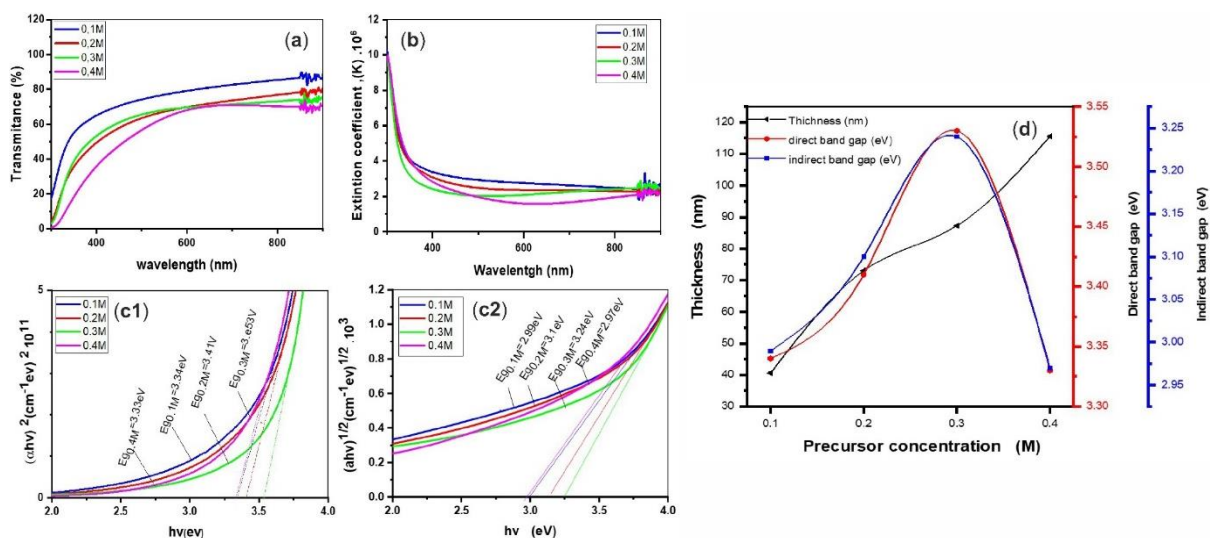


**Fig. 6.** a) Optical transmittance spectrum of  $\text{Bi}_2\text{O}_3$  synthesized by the different precursor concentrations. b) Variation of extinction coefficient ( $k$ ) versus wavelength with various molar concentrations. c1) Direct and c2) indirect band gap of the  $\text{Bi}_2\text{O}_3$  films. d) Variation of thickness and band gap with different precursor concentrations



Where  $d$  is film thickness, and  $I_0/I$  is the ratio of incident beam intensity to emergent beam [17, 30]. Band gap values are calculated from absorption spectra, and the method was described in previous literature [45]. The data were analyzed using the following classical relationship for optical transitions:

$$(\alpha h\nu)^2 = A(h\nu - E_g)^n \quad (6)$$

Where  $\alpha$ ,  $h$ ,  $\nu$ ,  $E_g$ , and  $A$  are the absorption coefficient, Planck constant, light frequency, band gap energy, and  $a$  is constant, respectively [46, 47]. There are two types of band gaps: direct band gaps and indirect band gaps; an electron can emit a photon directly in a direct band gap but not in an indirect band gap because the electron must pass through an intermediate state to transfer momentum to the crystal lattice [46]. The estimated direct and indirect transition band-gap values are demonstrated in Fig. 6(c1, c2), which shows the variation of direct and indirect band-gap values with different precursor concentrations. Both the direct and indirect band gap energies increased as the precursor concentration increased from 0.1 to 0.3 M, and then they decreased at 0.4 M; these results were

related to the transmittance of the films. The direct and indirect band gaps of the  $\text{Bi}_2\text{O}_3$  films with precursor concentrations of 0.1 and 0.4 M were the lowest; on the other hand, 0.2 and 0.3M were the highest. The extinction coefficient ( $k$ ) can be obtained from the relation [48]:

$$K = \alpha\lambda / 4. \pi \quad (7)$$

The variation of extinction coefficient with wavelength is shown in Fig. 6(b). The extinction coefficient was high in the 300–400 nm range and low in the 400–900 nm range. The rise in the extinction coefficient is directly related to light absorption.

### 3.5. Wettability Analysis

The wetting behavior of a solid surface in contact with water is determined by the interfacial tension between the surrounding medium (usually air) and water. When a surface exhibits high wettability, it tends to have a low contact angle, indicating that it is hydrophilic and readily interacts with water. Conversely, when the wettability is low, the contact angle is high, suggesting that the surface is hydrophobic and repels water [43, 49]. In the case of  $\text{Bi}_2\text{O}_3$  films, as depicted in Fig. 7, water contact angle measurements were conducted.

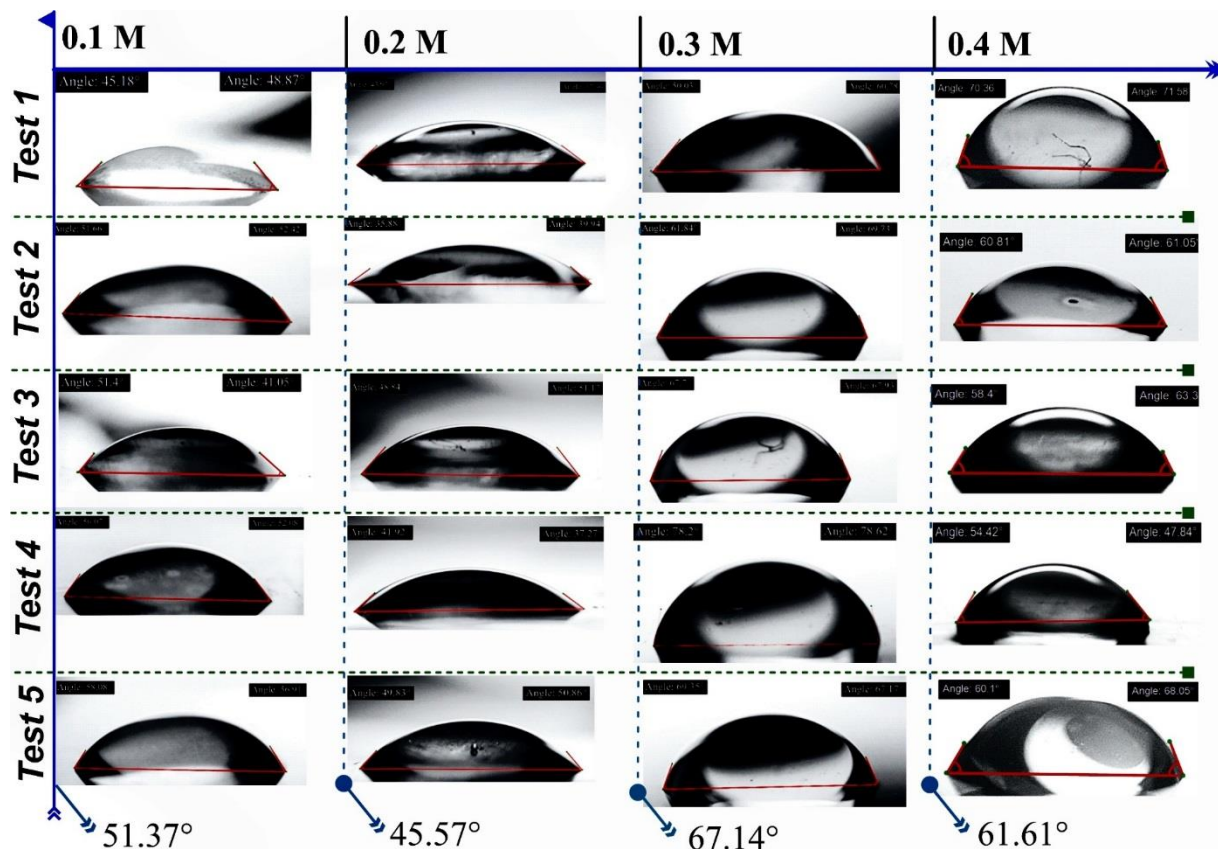


Fig. 7. Contact angle measurements images of  $\text{Bi}_2\text{O}_3$  thin films



The average contact angles for the samples with concentrations of 0.1 M, 0.2 M, 0.3 M, and 0.4 M were found to be 51.37°, 45.57°, 67.14°, and 61.61°, respectively, as illustrated in Fig. 8.

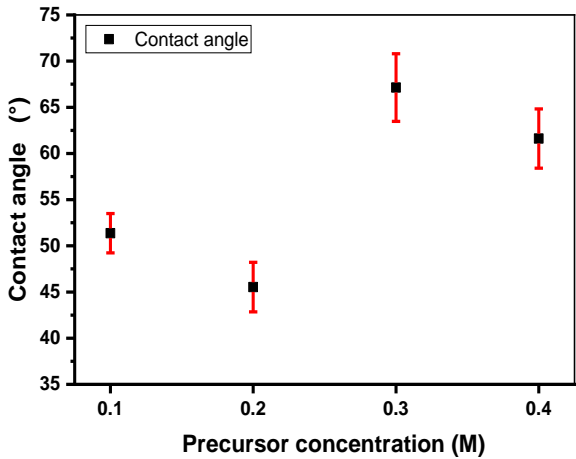


Fig. 8. Average distilled water (H<sub>2</sub>O) contact angles on the Bi<sub>2</sub>O<sub>3</sub> substrates

These results indicate that all the films are hydrophilic, implying a strong affinity for water. This hydrophilic property facilitates the interaction of the photocatalysts with

contaminants in water, leading to improved degradation performance [50].

3.6. The Photocatalytic Efficiency

The photocatalytic efficiency of Bi<sub>2</sub>O<sub>3</sub> thin films synthesized with variable precursor concentrations was evaluated by MB (2 ppm) photobleaching in an aqueous solution. Table. 4 shows the temperature, wind, and humidity variation for each hour. Fig. 9(a) shows the time-dependent visible light photocatalysis of thin films (0.1, 0.2, 0.3, 0.4 M), which decomposes the MB dye with a total exposure time of 4 h.

The absorbance edge of MB dye at 664 nm was decreased with increasing sunlight irradiation time. The degradation rate of MB dye is revealed in the presence of thin films as a catalyst. The following equation was used to calculate the photo degradation rate [51]:

$$D = A_0 - A_t / A_0 * 100 \% \tag{8}$$

Where A<sub>0</sub> is the initial absorbance at time t= 0 h, and A<sub>t</sub> is the absorbance after time t. The absorbance of MB dye over the Bi<sub>2</sub>O<sub>3</sub> thin films under sun irradiation for 4 h is shown in Fig. 9(d(1, 2, 3, and 4)).

Table 4. Change in temperature, wind, humidity, and solar radiation per hour in the BM degradation test (Biskra, Algeria) on 20 April 2021

Time (h)	0	1	2	3	4
Day temp (C <sup>0</sup> )	25	26	27	27	28
Wind speed (km/h)	12	11	10	9	9
Humidity (%)	41	40	38	37	35
Radiation amount	moderate				

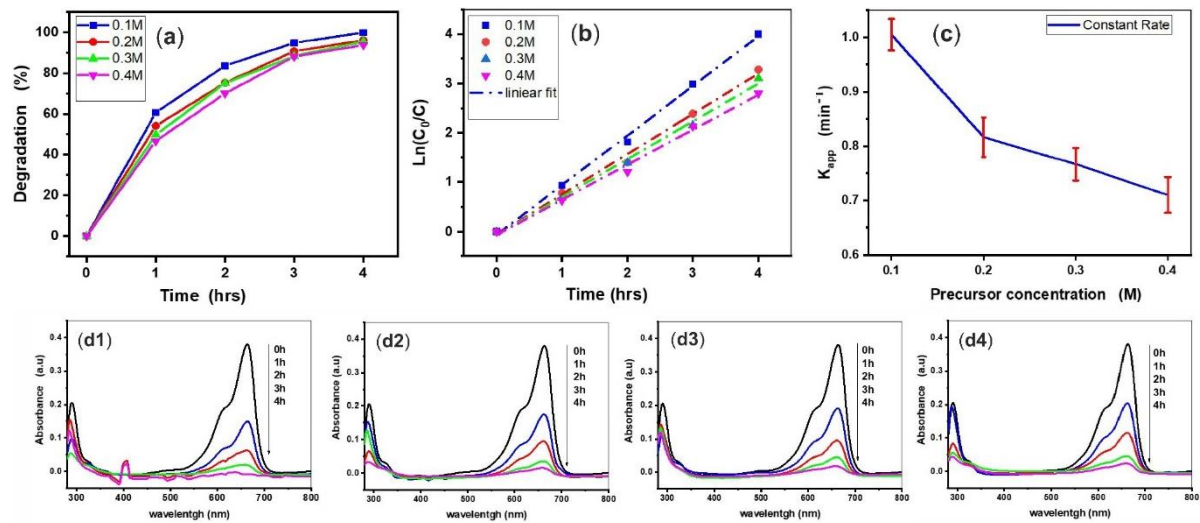
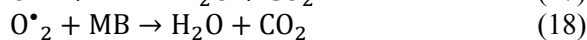
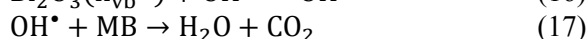
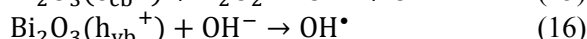
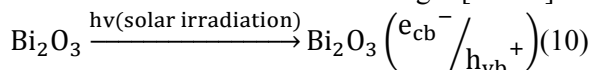


Fig. 9. a) The degradation rate of MB dye by Bi<sub>2</sub>O<sub>3</sub> thin films. b) Photocatalytic kinetics for all Bi<sub>2</sub>O<sub>3</sub> thin films. c) Effects of varying precursor concentrations of Bi<sub>2</sub>O<sub>3</sub> thin films on MB removal under irradiation time. Absorbance spectra of the MB solutions by Bi<sub>2</sub>O<sub>3</sub> thin films prepared with different precursor concentrations: d1) 0.1, d2) 0.2, d3) 0.3, and d4) 0.4 M

It was observed that after 2 h, the relative amounts of MB decomposed by photocatalysis were 47.09, 49.47, 53.97, and 83.60% when  $\text{Bi}_2\text{O}_3$  synthesized at 0.1, 0.3, 0.4, and 0.5 M was used as the photocatalyst, respectively.  $\text{Bi}_2\text{O}_3$  thin films prepared at 0.1 M have the highest photocatalytic efficiency among all samples, with 99.9% at 4 h irradiation time. The L-H kinetic mode can generally explain the kinetics of the photocatalytic degradation process [52].

$$\ln(C_0/C_t) = kt \quad (9)$$

Where  $C_0$  is the concentration at time  $t_0$ ,  $C_t$  is the concentration at a particular irradiation time, and  $k$  is the apparent pseudo-first-order rate constant ( $\text{min}^{-1}$ ). The apparent rate constant ( $k$ ) was successfully calculated from the slopes of the straight line obtained from the plot of natural logarithm by plotting the  $\ln(C_0/C_t)$  vs irradiation time [31]. The plot of  $-\ln(C/C_0)$  as a function of irradiation time for films  $\text{Bi}_2\text{O}_3$  prepared by different precursor molarities is presented in Fig. 9(b). Fig. 9(c) shows the kinetic rate of degradation of the dye solutions with increasing amounts of bismuth precursor. As observed, the highest kinetic rate decreases with increasing molar precursors, so the highest rate, 99.9%, is exhibited by 0.1 M. The following equations outline the photocatalytic attributes of  $\text{Bi}_2\text{O}_3$  films within an MB solution under sunlight [53–55]:



When bismuth oxide is activated with visible light ( $\lambda \geq 420$  nm), electrons are promoted from the valence band to the conduction band, generating an electron/hole pair ( $e^-/h^+$ ). (Eq. (10)) which are strong oxidizing and reducing agents, as shown in Fig. 10 [56]. Table 5 presents a thorough comparative examination between the current study and other research papers incorporating thin films and powders as a pivotal element in their investigations assessing the efficacy of photocatalysts in organic dye degradation.

The photo-induced holes are powerful oxidizers because of their attraction to electrons. They oxidize the adsorbed water molecule or hydroxide ion to produce hydroxyl radicals (Eq. 13). On the other hand, the electron from the photoexcitation attacks the oxygen (Eq. 11), it can be reduced to the different oxygen activated species (Eq. 11), Then all these highly oxidizing species ( $-\text{OH}$ ,  $\bullet\text{OH}$ ,  $\text{H}_2\text{O}_2$ , etc.) are capable of oxidizing organic molecules, such as MB into simpler molecules such as  $\text{CO}_2$ ,  $\text{H}_2\text{O}$  [57, 58].

#### 4. CONCLUSIONS

In this study,  $\text{Bi}_2\text{O}_3$  films are deposited using the sol-gel technique. The structural, morphological, optical, and photocatalytic properties of  $\text{Bi}_2\text{O}_3$  thin films were investigated as a function of precursor concentrations. The films are polycrystalline with a tetragonal structure peak as a preferred orientation.



Fig. 10. Illustrates the photocatalytic mechanisms of  $\text{Bi}_2\text{O}_3$  films for MB degradation under sunlight irradiation

**Table 5.** Illustrates a comparison between the photocatalytic efficiency of organic dye degradation observed in this investigation and findings from other studies

materials	Dye type and concentration	Technique type	Degradation (%)	Time (min)	Irradiation Source	Reference
$\beta$ -Bi <sub>2</sub> O <sub>3</sub> (0.1M), Thin film	Methylene blue, 0.002 g/l	Dip-coating (glass Substrate)	~99	240	Visible light	Current study
$\beta$ -Bi <sub>2</sub> O <sub>3</sub> , Thin film	Methylene blue, 10 <sup>-6</sup> mol/l	Spin-coating Deposition (Pt-coated silicon substrates)	~100	1440	Solar lamp (Ultra-Vitalux 300 W, Osram)	[59]
$\beta$ -Bi <sub>2</sub> O <sub>3</sub> , Powder	RhB, 5 mg/L	Situ chemical transformation method	~7	25	Xe lamp (350 W)	[60]
BiOBr, Powder	RhB, 5 mg/L	Situ chemical transformation method	~30	25	Xe lamp (350 W)	[60]
Co <sub>3</sub> O <sub>4</sub> (Co-3), Thin film	Methylene orange, 0.01 g/l	Nebulizer spray (glass and FTO Substrate)	~57	180	Tungsten Halogen lamp of 300 W (l >400 nm)	[61]
Co <sub>3</sub> O <sub>4</sub> (withdrawn speed of 5 mm/s), Thin film	Methylene blue, 0.002 g/l	Dip-coating (glass Substrate)	~77	240	Visible light	[62]
CuO/ZnO (simple A), Thin film	Methylene blue, 0.005 g/l	Spin-coating with Glass Substrate	~44	120	Xe lamp of 150 W	[63]
ZnO, Thin film	Methylene blue, 0.003 g/l	Spraying (glass Substrate)	~80	360	Visible light	[64]
CoTiO <sub>3</sub> /Co <sub>3</sub> O <sub>4</sub> , Thin film	Indo Light Blue, 0.01 g/l	Doctor blade and spin coating (glass Substrate)	~29	60	Hg lamp of 250 W	[65]
Cu:Co (30:70), Thin film	Methylene blue, 0.003 g/l	Dip-coating (glass Substrate)	~49	240	Visible light	[7]

The crystallite size of Bi<sub>2</sub>O<sub>3</sub> films was not gradually affected by the change in precursor concentration or film thickness. The morphology of the Bi<sub>2</sub>O<sub>3</sub> surface indicates irregular and good overall coverage, which increases with increasing molar precursor concentration, which is supported by the Rq area roughness of the sample.

The optical spectrum shows that the transmission increases with decreasing precursor concentration, and the maximum average value of about 78% in the visible region is observed for film prepared with 0.1 M. The direct band-gap values varied between 3.33 and 3.53 eV, and the direct band gap varied between 2.97-3.24 eV when the precursor

concentration was from 0.1 to 0.4 M-the average contact angles. Measurements proved the hydrophilic nature of the films as a contact angle between 51.37° and 61.61°. The degradation of MB decreases with the increase in precursor concentration, and the kinetic rate of degradation and degradation rate also have the highest values among all the thin films. Thus, the Bi<sub>2</sub>O<sub>3</sub> thin film of 0.1 M shows the fastest apparent photocatalytic reaction rate MB, at 99.9%, corresponding to 39.7 nm crystal size, 2.01 eV band gap energy, 55 nm surface roughness, and 51.37° contact angle. From the above results, it can be concluded that this Bismuth oxide film is a promising



photocatalyst for water purification.

## COMPETING INTERESTS

The authors report no financial or personal interests in this work.

## ETHICAL APPROVAL

Not applicable.

## INFORMED CONSENT

Not applicable.

## AUTHORS' CONTRIBUTIONS

All of the authors have studied this work.

## FUNDING

The authors have reported that they did not receive any funding.

## AVAILABILITY OF DATA AND MATERIALS

The corresponding author can access the statement regarding the datasets used in this work.

## ACKNOWLEDGMENTS

The authors would like to thank the Algerian Directorate General for Scientific Research and Technological Development-DGRSDT for financial assistance.

The authors wish to thank Mr. Saâd Rahmane and Mr. Brahim Gasmi for their assistance in XRD data acquisition from (LPCMA), University of Biskra, Algeria, and Pr. Tibarmacine from the University of Biskra, Algeria.

## REFERENCES

- [1]. Kiwaan, H. A., Atwee, T. M., Azab, E. A., El-Bindary, A. A., "Photocatalytic degradation of organic dyes in the presence of nanostructured titanium dioxide." *J. Mol. Struct.*, 2020, 1200, 115-127.
- [2]. Gamal Hasan, G., Khelef, A., Chaabia, N., Ali Mohammed, H., Laid Tedjani, M., Althamthami, M., "Fabrication and characterization of NFMA/FTO electrochemical thin film by electrodeposition and immersion techniques: An effective detector for H<sub>2</sub>O<sub>2</sub> and sunlight-driven MB degradation." *J. Photochem. Photobiol. A Chem.*, 2023, 445, 112-115.
- [3]. Hasan, G. G., Mohammed, H. A., Althamthami, M., Khelef, A., Laouini, S. E., Meneceur, S., "Synergistic effect of novel biosynthesis SnO<sub>2</sub>@Fe<sub>3</sub>O<sub>4</sub> nanocomposite: A comprehensive study of its photocatalytic of Dyes & antibiotics, antibacterial, and antimutagenic activities." *J. Photochem. Photobiol. A Chem.*, 2023, 443, 114-874.
- [4]. Omidvar, A., Jaleh, B., Nasrollahzadeh, M., "Preparation of the GO/Pd nanocomposite and its application for the degradation of organic dyes in water." *J. Colloid Interface Sci.*, 2017, 496, 44–50.
- [5]. Nuengmatcha, P., Porrawatkul, P., Chanthai, S., Sricharoen, P., Limchoowong, N., "Enhanced photocatalytic degradation of methylene blue using Fe<sub>2</sub>O<sub>3</sub>/graphene/CuO nanocomposites under visible light." *J. Environ. Chem. Eng.*, 2019, 7, 103-438.
- [6]. Yang, L., Chen, C., Hu, Y., Wei, F., Cui, J., Zhao, Y., Xu, X., Chen, X., Sun, D., "Three-dimensional bacterial cellulose/polydopamine/TiO<sub>2</sub> nanocomposite membrane with enhanced adsorption and photocatalytic degradation for dyes under ultraviolet-visible irradiation." *J. Colloid Interface Sci.*, 2020, 562, 21–28.
- [7]. Althamthami, M., Elhachmi, G. T., Ben Temam, H., Hasan, G. G., Rahmane, S., Gasmi, B., "Effect of Different Cu:Co Film Concentrations on Photocatalytic Reactions of Ethanol, MB, AMX, and Cr(VI): A Study of Film Properties & Effects of Photooxidation." *J. Environ. Chem. Eng.*, 2023, 111-247.
- [8]. Reddy, C. V., Reddy, I. N., Harish, V. V. N., Reddy, K. R., Shetti, N. P., Shim, J., Aminabhavi, T. M., "Efficient removal of toxic organic dyes and photoelectrochemical properties of iron-doped zirconia nanoparticles." *Chemosphere*, 2020, 239, 124-766.
- [9]. Akhtar, J., Tahir, M. B., Sagir, M., Bamufleh, H. S., "Improved photocatalytic performance of Gd and Nd co-doped ZnO nanorods for the degradation of methylene blue." *Ceram. Int.*, 2020, 46, 11955–11961.
- [10]. Kumari, V., Mittal, A., Jindal, J., Yadav, S., Kumar, N., "S-, N- and C-doped ZnO as

- semiconductor photocatalysts: A review." *Front Mater Sci.*, 2019, 13.
- [11]. Kabra, K., Chaudhary, R., Sawhney, R. L., "Treatment of hazardous organic and inorganic compounds through aqueous-phase photocatalysis: A review." *Ind. Eng. Chem. Res.*, 2004, 43, 7683–7696.
- [12]. Soares, L., Alves, A., "Photocatalytic properties of  $\text{TiO}_2$  and  $\text{TiO}_2/\text{WO}_3$  films applied as semiconductors in heterogeneous photocatalysis." *Mater. Lett.*, 2018, 211, 339–342.
- [13]. Li, J. Z., Zhong, J. B., Zeng, J., Feng, F. M., He, J. J., "Improved photocatalytic activity of dysprosium-doped  $\text{Bi}_2\text{O}_3$  prepared by sol-gel method." *Mater. Sci. Semicond. Process.*, 2013, 16, 379–384.
- [14]. Xiaohong, W., Wei, Q., Weidong, H., "Thin bismuth oxide films prepared through the sol-gel method as photocatalyst." 2007, 261, 167–171.
- [15]. Orozco-Hernández, G., Olaya-Flórez, J., Pineda-Vargas, C., Alfonso, J. E., Restrepo-Parra, E., "Structural, chemical and electrochemical studies of bismuth oxide thin films growth via Unbalanced Magnetron Sputtering." *Surfaces and Interfaces*, 2020, 21, 100-627.
- [16]. Dev, B. C., Babu, M. H., Podder, J., Sagadevan, S., Zubair, A., "Low temperature synthesis of  $\alpha$ - and  $\beta$ -phase  $\text{Bi}_2\text{O}_3$  thin film via B doping: tailoring optical band gap and n- to p-type  $\text{Bi}_2\text{O}_3$ ." *J. of Mater. Sci.: Mater. in Ele.*, 2019, 30, 15670–15682.
- [17]. Dapčević, A., Poleti, D., Rogan, J., Radojković, A., Radović, M., Branković, G., "A new electrolyte based on  $\text{Tm}^{3+}$ -doped  $\delta$ - $\text{Bi}_2\text{O}_3$ -type phase with enhanced conductivity." *Sol. Sta. Ion.*, 2015, 280, 18–23.
- [18]. Fan, H. T., Pan, S. S., Teng, X. M., Ye, C., Li, G. H., Zhang, L. D., " $\delta$ - $\text{Bi}_2\text{O}_3$  thin films prepared by reactive sputtering: Fabrication and characterization." *Thin Solid Films*, 2006, 513, 142–147.
- [19]. Zhu, B. L., Zhao, X. Z., "Study on structure and optical properties of  $\text{Bi}_2\text{O}_3$  thin films prepared by reactive pulsed laser deposition." *Opt. Mater. (Amst.)*, 2006, 29, 192–198.
- [20]. Hettal, S., Ouahab, A., Rahmane, S., Benmessaoud, O., Sayad, M., "Properties of Copper Oxide Thin Films Deposited by Sol-Gel Dip-Coating Technique." *Iranian Journal of Materials Science and Engineering*, 2022, 19, 1–8.
- [21]. Sun, Z., Oka, D., Fukumura, T., "Epitaxial Growth of  $\beta$ - $\text{Bi}_2\text{O}_3$  Thin Films and Particles with Mist Chemical Vapor Deposition." *Cryst. Growth Des.*, 2019, 19, 7170–7174.
- [22]. Wu, S., Fang, J., Xu, W., Cen, C., "Hydrothermal synthesis, characterization of visible-light-driven  $\alpha$ - $\text{Bi}_2\text{O}_3$  enhanced by  $\text{Pr}^{3+}$  doping". *Journal of Chemical Technology and Biotechnology*, 2013, 88, 1828–1835.
- [23]. Tong, Y., Jiang, B., Chen, X., Ren, X., Lu, J., Ding, L., "Synergistic degradation of methylene blue by laser cavitation and activated carbon fiber." *Opt. Laser Technol.*, 2022, 155, 108-417.
- [24]. Chen, M. L., Li, S. S., Wen, L., Xu, Z., Li, H. H., Ding, L., Cheng, Y. H., "Exploration of double Z-type ternary composite long-afterglow/graphitic carbon nitride@metal-organic framework for photocatalytic degradation of methylene blue." *J. Colloid Interface Sci.*, 2023, 629, 409–421.
- [25]. Arif, M., Liu, G., Yousaf, B., Ahmed, R., Irshad, S., Ashraf, A., Zia-ur-Rehman, M., Rashid, M. S., "Synthesis, characteristics and mechanistic insight into the clays and clay minerals-biochar surface interactions for contaminants removal-A review." *J. Clean Prod.*, 2021, 310, 127-548.
- [26]. El-Ghobashy, M. A., Salem, I. A., El-Dahrawy, W. M., Salem, M. A., "Fabrication of  $\alpha$ - $\text{MnO}_2/\text{Fe-Mn}$  binary oxide nanocomposite as an efficient adsorbent for the removal of methylene blue from wastewater." *J. Mol. Struct.*, 2023, 1272, 118-134.
- [27]. Baqiah, H., Talib, Z. A., Liew, J. Y. C., Shaari, A. H., Zainal, Z., F, L. M., "Effects of precursor concentration on the microstructural, optical and photoelectrochemical properties of  $\text{Bi}_2\text{O}_3$  films synthesized by sol-gel method." *Optik. (Stuttg.)*, 2020, 206.
- [28]. Weidong, H., Wei, Q., Xiaohong, W., Hailong, N., "Thin bismuth oxide films prepared through the sol-gel method."

- 2007, 61, 4100–4102.
- [29]. Althamthami, M., Guettaf Temam, E., Ben Temam, H., Hasan, G. G., Malfi, N., "Influence of hole-scavenger and different withdrawn speeds on photocatalytic activity of  $\text{Co}_3\text{O}_4$  thin films under sunlight irradiation." *Ceram. Int.*, 2022, 48, 31570–31578.
- [30]. Althamthami, M., Guettaf Temam, E., Temam, H. Ben, Saad, R., Hasan, G. G., "Improved photocatalytic activity under the sunlight of high transparent hydrophilic Bi-doped  $\text{TiO}_2$  thin-films." *J. Photochem. Photobiol. A Chem.*, 2023, 443, 114-818.
- [31]. Raza, W., Bahnemann, D., Muneer, M., "A green approach for degradation of organic pollutants using rare earth metal doped bismuth oxide." *Catal. Today*, 2018, 300, 89–98.
- [32]. Jadhav, C. H., Pagare, P. K., Inamdar, K. K., Kadam, L. D., "Preparation of Bismuth Oxide Thin Films by Spray Pyrolysis Method and Its Characterizations." *Macromol. Symp.*, 2019, 387, 1–3.
- [33]. Seid, E. T., Dejene, F. B., Urgessa, Z. N., Botha, J. R., "Refluxed sol–gel synthesized  $\text{ZnO}$  nanopowder with variable zinc precursor concentrations." *Appl. Phys. A Mater. Sci. Process*, 2018, 124, 1–13.
- [34]. Ravishankar, S., Balu, A. R., Anbarasi, M., Nagarethinam, V. S., "Influence of precursor molar concentration on the structural, morphological, optical and electrical properties of  $\text{PbS}$  thin films deposited by spray pyrolysis technique using perfume atomizer." *Optik. (Stuttg.)*, 2015, 126, 2550–2555.
- [35]. Kamble, D. L., Harale, N. S., Patil, V. L., Patil, P. S., Kadam, L. D., "Characterization and  $\text{NO}_2$  gas sensing properties of spray pyrolyzed  $\text{SnO}_2$  thin films." *J. Anal. Appl. Pyrolysis.*, 2017, 127, 38–46.
- [36]. Seid, E. T., Dejene, F. B., Urgessa, Z. N., Botha, J. R., "Refluxed sol–gel synthesized  $\text{ZnO}$  nanopowder with variable zinc precursor concentrations." *Appl. Phys. A Mater. Sci. Process*, 2018, 124, 1–13.
- [37]. Aryanto, D., Jannah, W. N., Masturi, Sudiro, T., Wismogroho, A. S., Sebayang, P., Sugianto, Marwoto, P., "Preparation and structural characterization of  $\text{ZnO}$  thin films by sol-gel method." *J. Phys. Conf. Ser.*, 2017, 817, 012-025.
- [38]. Pérez-González, M., Tomás, S. A., Santoyo-Salazar, J., Morales-Luna, M., "Enhanced photocatalytic activity of  $\text{TiO}_2$ - $\text{ZnO}$  thin films deposited by dc reactive magnetron sputtering." *Ceram. Int.*, 2017, 43, 8831–8838.
- [39]. Kamaruddin, S. A., Chan, K. Y., Yow, H. K., Zainizan Sahdan, M., Saim, H., Knipp, D., "Zinc oxide films prepared by sol-gel spin coating technique." *Appl. Phys. A Mater. Sci. Process*, 2011, 104, 263–268.
- [40]. Ravishankar, S., Balu, A. R., Anbarasi, M., Nagarethinam, V. S., "Influence of precursor molar concentration on the structural, morphological, optical and electrical properties of  $\text{PbS}$  thin films deposited by spray pyrolysis technique using perfume atomizer." *Optik. (Stuttg.)*, 2015, 126, 2550–2555.
- [41]. Kouidri, Nabila, Rahmane, Saâd, "Effect of Cobalt Chloride Concentration on Structural, Optical and Electrical Properties of  $\text{Co}_3\text{O}_4$  Thin Films Deposited by Pneumatic Spray." *Journal of New Technology and Materials*, 2020, 10, 56–62.
- [42]. Sbeta, M., Atilgan, A., Atli, A., Yildiz, A., "Influence of the spin acceleration time on the properties of  $\text{ZnO:Ga}$  thin films deposited by sol–gel method." *J. Solgel. Sci. Technol.*, 2018, 86, 513–520.
- [43]. Shaikh, A. A., Waikar, M. R., Sonkawade, R. G., "Effect of different precursors on electrochemical properties of manganese oxide thin films prepared by SILAR method." *Synth. Met.*, 2019, 247, 1–9.
- [44]. Guettaf Temam, E., Djani, F., Rahmane, S., Ben Temam, H., Gasmi, B., "Photocatalytic activity of  $\text{Al/Ni}$  doped  $\text{TiO}_2$  films synthesized by sol-gel method: Dependence on thickness and crystal growth of photocatalysts." *Surfaces and Interfaces*, 2022, 31, 077-102.
- [45]. Xiaohong, W., Wei, Q., Li, L., Yun, G., Zhaoyang, X., "Photocatalytic property of nanostructured  $\text{Fe}^{3+}$ -doped  $\text{Bi}_2\text{O}_3$  films." *Catal. Commun.*, 2009, 10, 600–604.
- [46]. Qin, W., Qi, J., Wu, X., "Photocatalytic property of  $\text{Cu}^{2+}$ -doped  $\text{Bi}_2\text{O}_3$  films under visible light prepared by the sol gel



- method." *Vaccum*, 2014, 3–6.
- [47]. Mokrani, N., Guettaf Temam, E., Barkat, H., Ben Temam, H., Rahmane, S., Althamthami, M., "Boosting photocatalytic stability: hydrophilic Sr-doped ZnO thin films prepared via the SILAR method for enhanced performance over multiple cycles." *Phys. Scr.*, 2024, 99, 094-095.
- [48]. Jothibas, M., Manoharan, C., Dhanapandian, S., Jeyakumar, S. J., "Influence of precursor concentration on sprayed  $\text{In}_2\text{O}_3$  thin films." *Asian Journal of Chemistry*, 2013, 25.
- [49]. Althamthami, M., Temam, G., Hachmi, E. I., Temam, H. Ben, Hasan, G. G., Gasmi, B., Hasan, G., Rahmane, S., "Tailor-made Tenorite ( $\text{CuO}$ ) Interface Films for Enhanced Photocatalysis: An Improved Dip-Coating Approach with Enhanced Surface Topography and Hydrophobicity." 2023, 1.
- [50]. Lu, H., Hao, Q., Chen, T., Zhang, L., Chen, D., Ma, C., Yao, W., Zhu, Y., "A high-performance  $\text{Bi}_2\text{O}_3/\text{Bi}_2\text{SiO}_5$  p-n heterojunction photocatalyst induced by phase transition of  $\text{Bi}_2\text{O}_3$ ." *Appl. Catal. B*, 2018, 237, 59–67.
- [51]. Begum, S., Ahmaruzzaman, M., "Green Synthesis of  $\text{SnO}_2$  Nanoparticles loaded on Activated Carbon and its Application as Photocatalyst in the Degradation of Alizarin Red S Dye." *Mater. Today Proc.*, 2018, 5, 2314–2320.
- [52]. Islam, M. R., Rahman, M., Farhad, S. F. U., Podder, J., "Structural, optical and photocatalysis properties of sol–gel deposited Al-doped ZnO thin films." *Surfaces and Interfaces*, 2019, 16, 120–126.
- [53]. Li, J., Guo, J., Zhang, J., Sun, Z., Gao, J., "Surface etching and photodeposition nanostructures core-shell  $\text{Cu}_2\text{O}@\text{CuO}-\text{Ag}$  with S-scheme heterojunction for high efficiency photocatalysis." *Surfaces and Interfaces*, 2022, 34, 102-308.
- [54]. Tornabene, F., Triantafillou, T., Teklemariam Gaim, Y., Mekides Yimanuh, S., Girmay Kidanu, Z., "Enhanced Photocatalytic Degradation of Amoxicillin with Mn-Doped  $\text{Cu}_2\text{O}$  under Sunlight Irradiation." *Journal of Composites Science*, 2022, 6, 317.
- [55]. Balarak, D., Mengelizadeh, N., Rajiv, P., Chandrika, K., "Photocatalytic degradation of amoxicillin from aqueous solutions by titanium dioxide nanoparticles loaded on graphene oxide." *Environmental Science and Pollution Research*, 2021, 28, 49743–49754.
- [56]. Kusuma, K. B., Manju, M., Ravikumar, C. R., Dileepkumar, V. G., Kumar, A. N., Santosh, M. S., Murthy, H. C. A., Gurushantha, K., "Probe Sonicated Synthesis of Bismuth Oxide ( $\text{Bi}_2\text{O}_3$ ): Photocatalytic Application and Electrochemical Sensing of Ascorbic Acid and Lead." *J. Nanomater.*, 2022.
- [57]. Zahid, A. H., Han, Q., Jia, X., Li, S., Hangjia, H., Liu, H., "Highly stable 3D multilayered nanoparticles-based  $\beta\text{-Bi}_2\text{O}_3$  hierarchitectre with enhanced photocatalytic activity." *Opt. Mater. (Amst.)*, 2020, 109, 110-389.
- [58]. Abu-Dief, A. M., Mohamed, W. S., " $\alpha\text{-Bi}_2\text{O}_3$  nanorods: synthesis, characterization and UV-photocatalytic activity." *Mater. Res. Express*, 2017, 4, 035-039.
- [59]. Perez-Mezcua, D., Bretos, I., Jiménez, R., Ricote, J., Jiménez-Rioboó, R. J., da Silva, C. G., Chateigner, D., Fuentes-Cobas, L., Sirera, R., Calzada, M. L., "Photochemical solution deposition of  $\beta\text{-Bi}_2\text{O}_3$  thin films." *J. Solgel. Sci. Technol.*, 2017, 81, 355–361.
- [60]. Wu, S., Xie, Y., Zhang, X., Huang, Z., Liu, Y., Fang, M., Wu, X., Min, X., "In situ synthesis of adsorptive  $\beta\text{-Bi}_2\text{O}_3/\text{BiOBr}$  photocatalyst with enhanced degradation efficiency." *J. Mater. Res.*, 2019, 34, 3450–3461.
- [61]. Ravi Dhas, C., Venkatesh, R., David Kirubakaran, D., Princy Merlin, J., Subramanian, B., Moses Ezhil Raj, A., "Electrochemical sensing of glucose and photocatalytic performance of porous  $\text{Co}_3\text{O}_4$  films by nebulizer spray technique." *Mater. Chem. Phys.*, 2017, 186, 561–573.
- [62]. Althamthami, M., Guettaf Temam, E., Ben Temam, H., Hasan, G. G., Malfi, N., "Influence of hole-scavenger and different withdrawn speeds on photocatalytic activity of  $\text{Co}_3\text{O}_4$  thin films under sunlight irradiation." *Ceram. Int.*, 2022, 48, 31570–31578.
- [63]. Xu, L., Su, J., Zheng, G., Zhang, L.,

- "Enhanced photocatalytic performance of porous ZnO thin films by CuO nanoparticles surface modification." *Materials Science and Engineering: B*, 2019, 248, 114-405.
- [64]. Mrabet, C., Jaballah, R., Mahdhi, N., Boukhachem, A., Amlouk, M., "CuO-ZnO nanocomposites-based thin films: Characterization, physical properties and sunlight photocatalytic degradation of organic pollutants." *J. Alloys. Compd.*, 2023, 968, 172-252.
- [65]. Habibi, M. H., Shojaei, E., "Synthesis of a heterojunction CoTiO<sub>3</sub>/Co<sub>3</sub>O<sub>4</sub> nanocomposite thin film with superior photocatalytic activity and reusability: Effect of calcination temperature on phase transformation and effect of oxidants on enhanced degradation of Indo Light Blue dye." *Spectrochim. Acta A Mol Biomol. Spectrosc.*, 2020, 229, 117-796.